

A first-principles study of structural, elastic, electronic, and transport properties of Cs₂Te

Gaoxue Wang^a, Jinlin Zhang^b, Chengkun Huang^a, Dimitre A. Dimitrov^b, Anna M. Alexander^b, and Evgenya I Simakov^b

^aTheoretical Division, Los Alamos National Laboratory P.O. Box 1663, Los Alamos, NM 87545, USA

^bAOT-AE, Los Alamos National Laboratory P.O. Box 1663, Los Alamos, NM 87545, USA

Abstract

The pursuit to operate photocathodes at high accelerating gradients to increase brightness of electron beams is gaining interests within the accelerator community. Cesium telluride (Cs₂Te) is a widely used photocathode material and it is presumed to offer resilience to higher gradients because of its wider band gap compared to other semiconductors. Despite its advantages, crucial material properties of Cs₂Te remain largely unknown both in theory and experiments. In this study, we employ first-principles calculations to provide detailed structural, elastic, electronic and transport properties of Cs₂Te. It is found that Cs₂Te has an intrinsic mobility of 20 cm²/Vs for electrons and 2.0 cm²/Vs for holes at room temperature. The low mobility is primarily limited by the strong polar optical phonon scattering. Cs₂Te also exhibits ultralow lattice thermal conductivity of 0.2 W/(m*K) at room temperature. Based on the energy gain/loss balance under external field and electron-phonon scattering, we predict that Cs₂Te has a dielectric breakdown field in the range from ~60 MV/m to ~132 MV/m at room temperature dependent on the doping level of Cs₂Te. Our results are crucial to advance the understanding of applicability of Cs₂Te photocathodes for high-gradient operation.

Corresponding author:
gaoxuew@lanl.gov

I. Introduction

In advanced photocathode community, there is a growing interest in applying high gradients to photocathodes to increase brightness of electron beams.[1, 2] One concern regarding the application of high gradients to semiconductor photocathodes is that they are susceptible to dielectric breakdown due to impact ionization.[3, 4] Impact ionization occurs when the electric field applied to a material exceeds a critical threshold, causing an abrupt increase in electrical conductivity. This phenomenon results from the acceleration of charge carriers in the material to velocities capable of creating additional free charge carriers through collisions. As a result, an avalanche process occurs, leading to a rapid increase in the number of free charge carriers and a significant decrease in the material's resistance. Such breakdown can result in failure of the device or degradation of performance.

It is reasoned that semiconducting cesium telluride (Cs_2Te) photocathode may be capable of withstanding higher electric fields due to the larger band gap of 3.3 eV in Cs_2Te compared to other semiconducting materials, such as alkali antimonide. Cs_2Te is a popular photocathode material because of its high quantum efficiency (QE) exceeding 10% at its working wavelength, long lifetimes over a span of several months, stability under various operating conditions, and relatively fast response times.[5] Cs_2Te photocathodes are in operational photoinjectors[6] for several major accelerator facilities such as LCLS-II (SLAC, USA), FLASH (DESY), and European XFEL (Germany), as well as in many smaller accelerators and test facilities worldwide.[7] At Los Alamos National Laboratory (LANL), we selected to use Cs_2Te to generate ultra-bright electron beam at the Cathodes and Radiofrequency Interactions in Extremes (CARIE) photocathode test stand.[8]

Despite its widespread use, many material properties of Cs_2Te relevant to its interactions with strong electromagnetic fields remain unknown. For instance, to the best of our knowledge, the electrical and thermal conductivities of Cs_2Te have never been reported in the literature. The electrical conductivity is crucial for understanding photocathode behavior, as poor electrical conductivity may result in ionized surfaces, impacting photoemission or even integrity of the photocathode.[9] Thermal conductivity is essential for heat dissipation during operation of photocathodes. Furthermore, the performance of Cs_2Te photocathodes under high gradients remains unclear and requires detailed understanding of the transport properties. Additionally, one quantity that is absolutely necessary to study is the dielectric breakdown field that Cs_2Te photocathodes can withstand and its dependence on RF frequency of the electromagnetic field.

In this study, we employ first-principles calculations based on density functional theory (DFT) and density functional perturbation theory (DFPT) to predict fundamental properties of Cs_2Te , including structural, elastic, vibrational, electronic and transport properties. We compute the electron-phonon and phonon-phonon scattering rates of Cs_2Te for the first time using first-principles approach, enabling the calculations of electron and phonon transport via the Boltzmann transport equation (BTE). Our calculations reveal that Cs_2Te has an ultralow thermal conductivity of 0.2 W/(m*K) due to its low group velocity, indicating that heat dissipation in Cs_2Te photocathodes will be inefficient, potentially impacting high power applications. We predict room-temperature intrinsic mobilities of 20 cm^2/Vs for electrons and 1.2 cm^2/Vs for holes, primarily limited by the strong polar optical phonon scattering.

Additionally, using the von Hippel low-energy criterion[10] the electron-phonon scattering rates allow us to estimate that the breakdown field varies in between 60 MV/m and 132 MV/m at room temperature depending on the doping level of Cs₂Te. These calculated results provide critical inputs for modeling Cs₂Te photocathodes, particularly regarding detailed photoemissive properties based on Monte Carlo simulations,[11-13], which are key to advance understanding of applicability of Cs₂Te photocathodes in high-gradient accelerators.

II. Crystal structure of Cs₂Te

To determine the crystal structure and atomic positions in Cs₂Te, we fully relaxed the lattice parameters and atomic coordinates using the Vienna ab-initio simulation package (VASP) [1, 2] based on DFT. The Perdew-Burke-Ernzerhof (PBE) [14] functional of the generalized gradient approximation (GGA) was used for the electron exchange-correlation. Standard PAW-PBE pseudopotentials [15] were used with a cutoff energy of 500 eV for the plane waves. The structure was converged with the maximum force on each atom smaller than 0.01 eV/Å. Cs₂Te belongs to the Pnma space group (no. 62) with an orthorhombic unit cell characterized by the three lattice vectors *a*, *b*, and *c*. The relaxation yielded lattice constants of *a*=9.62, *b*=5.89, *c*=11.63 Å. The comparison between the computed and measured lattice constants is shown in Table 1 [16, 17]. In Cs₂Te, Cs atoms occupy two inequivalent sites with different coordination and bond character, denoted as Cs_I and Cs_{II} in Figure 1(a). Cs_I is bonded with 5 neighboring Te atoms with bond length smaller than 4.5 Å. Cs_{II} is bonded with 4 Te atoms with a bond length smaller than 3.9 Å. The average Cs-Te bond length in Cs₂Te is approximately 3.95 Å.

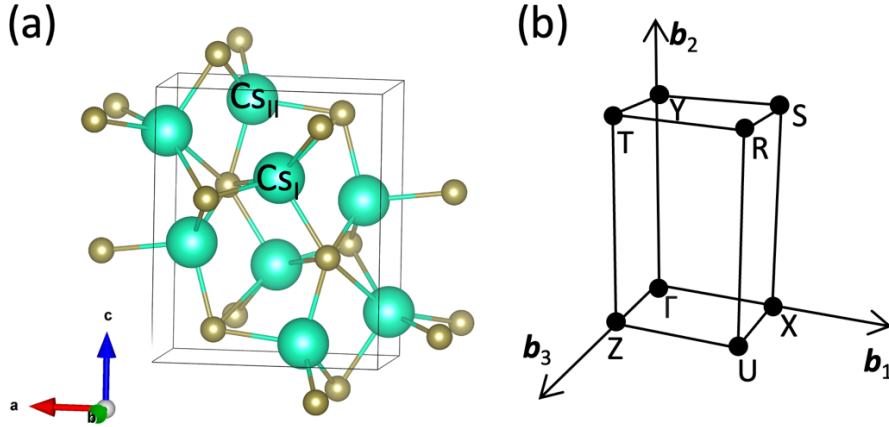


Figure 1. (a) Crystal structure of Cs₂Te where the larger atoms are Cs and the smaller atoms are Te. Cs_I and Cs_{II} denote Cs atoms that occupy two inequivalent sites. (b) the schematic of the Brillouin zone used in calculating the electronic band structure and the phonon dispersion. Rendered using VESTA.[18]

Table 1. Calculated and experimental lattice constants of Cs₂Te.

	This work	Experiment [16, 17]
<i>a</i>	9.62	9.512
<i>b</i>	5.89	5.838
<i>c</i>	11.63	11.748

III. Elastic properties of Cs₂Te

Elastic properties are crucial to know in numerous technological applications. They influence the fracture, toughness, and sound velocities in the material. While a crystal theoretically has 36 independent elastic constants, the inherent symmetry of the crystal significantly reduces the number of independent elastic constants. Cs₂Te has only eight independent elastic constants: C_{11} , C_{12} , C_{13} , C_{22} , C_{33} , C_{44} , C_{55} and C_{66} . These elastic constants can be averaged by integration on the unit sphere to calculate the standard Young modulus, bulk modulus, shear modulus, and Poisson's ratio. Utilizing the ELATE code,[19] we computed the elastic properties of Cs₂Te, which are presented in Table 2. The elastic constants clearly satisfy the Born stability criteria [20] for materials with orthorhombic structures: (i) $C_{11} > 0$; (ii) $C_{11} * C_{22} > C_{12}^2$; (iii) $C_{11} * C_{22} * C_{33} + 2C_{12} * C_{13} * C_{23} - C_{11} * C_{23}^2 - C_{22} * C_{13}^2 - C_{33} * C_{12}^2 > 0$; (iv) $C_{44} > 0$; (v) $C_{55} > 0$; (vi) $C_{66} > 0$. The calculated bulk modulus and shear modulus are 9.52 GPa and 3.72 GPa, respectively. The small bulk and shear moduli indicate Cs₂Te is a relatively soft material with weak chemical bonds, likely due to the large Cs-Te bond length as described in the previous section.

Table 2. Calculated elastic constants, bulk modulus B , shear modulus G , Young's modulus E , Poisson's ratio ν of Cs₂Te. The values reported in this table are from the Voigt-Reuss-Hill averaging approach.[21-23]

C_{11}	C_{12}	C_{13}	C_{22}	C_{33}	C_{44}	C_{55}	C_{66}	B	G	E	ν
(GPa)	(GPa)	(GPa)	(GPa)								
12.83	6.65	6.64	14.17	18.21	2.20	4.16	4.95	9.52	3.72	9.88	0.33

IV. Vibrational properties of Cs₂Te

We investigated the vibrational properties of Cs₂Te using density functional perturbation theory (DFPT). To ensure the convergence of the vibrational frequencies, we constructed a $1 \times 3 \times 1$ supercell for phonon dispersion calculations. A Monkhorst-Pack k -mesh of $2 \times 1 \times 2$ was used to sample the Brillouin zone (BZ). Harmonic second-order interatomic force constants (IFCs) were derived using the finite displacement method, utilizing force constants obtained from VASP calculations. Subsequently, we calculated the phonon dispersion of Cs₂Te using the PHONOPY package based on these IFCs.[24] Our calculated phonon dispersion, shown in Figure 2, reveals absence of imaginary frequencies, indicating the dynamical stability of the structure. The highest vibrational frequency is observed to be approximately 100 cm^{-1} at the Γ -point. Moreover, a discontinuity in the phonon dispersion near the Γ -point is evident, which is caused by the anisotropy of crystal structure. In our calculations, we considered the non-analytic term corrections, addressing the influence of the polarization field on the optical phonon behavior around the Γ -point. The strong anisotropy of the polarization along different directions leads to direction-dependent corrections, resulting in the discontinuity of the phonon dispersion at the Γ -point when the phonon wave vector changes direction.

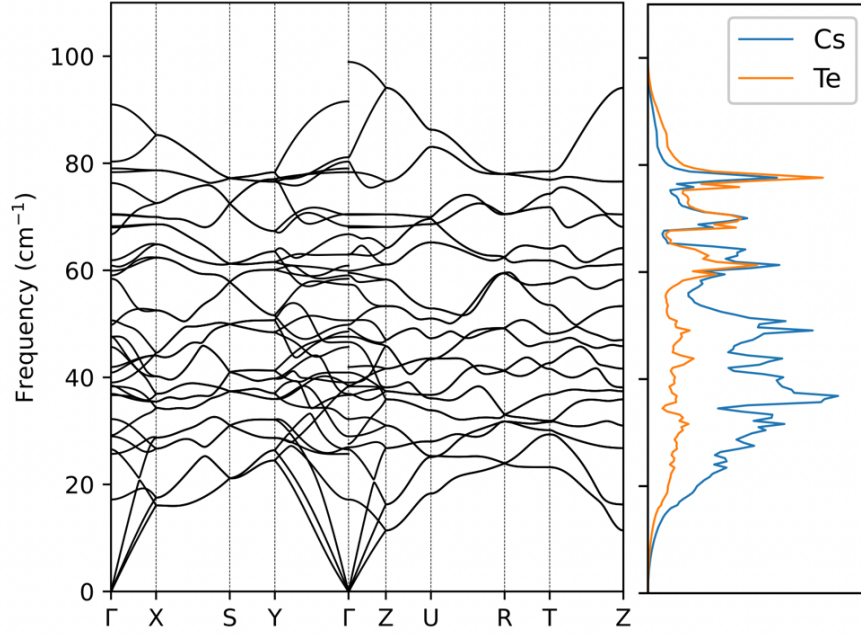


Figure 2. Phonon dispersion and phonon density of states of Cs_2Te .

The vibrational frequencies of each phonon mode at the Γ -point are listed in [Table 3](#). The Raman and Infrared activity of each mode are also shown in the Table. There are 18 Raman active mode ($6A_g+3B_{1g}+6B_{2g}+3B_{3g}$) and 12 Infrared active modes ($5B_{1u}+2B_{2u}+5B_{3u}$). These computed vibrational frequencies can be compared with experimental Raman/Infrared spectra to validate the quality of the grown Cs_2Te films.

Table 3. Phonon frequencies of Cs_2Te at the center of Brillouin zone (Γ -point), and their Raman/Infrared activity. The three zero-frequency acoustic modes are not included in the table.

Mode	Frequency (cm^{-1})	Activity
Au	17.18	-
B _{1u}	25.70	Infrared
A _g	26.54	Raman
B _{3g}	28.98	Raman
B _{3u}	29.18	Infrared
B _{1g}	32.21	Raman
A _g	36.69	Raman
B _{1g}	36.92	Raman
B _{2g}	38.31	Raman
Au	38.47	-
A _g	39.04	Raman
B _{3g}	40.90	Raman
B _{2u}	41.94	Infrared
B _{1u}	45.67	Infrared
B _{3u}	46.60	Infrared

B2g	47.60	Raman
Ag	49.82	Raman
B2g	50.66	Raman
B1u	58.42	Infrared
B2g	59.06	Raman
Ag	59.92	Raman
B1u	60.87	Infrared
B3u	61.88	Infrared
B2g	66.74	Raman
B2u	68.01	Infrared
Au	68.26	-
B3g	70.37	Raman
B1g	70.51	Raman
B3u	76.31	Infrared
Ag	78.34	Raman
B1u	79.03	Infrared
B2g	80.32	Raman
B3u	90.99	Infrared

V. Lattice thermal conductivity of Cs₂Te

Thermal conductivity plays a pivotal role in managing heat within high-power devices and is of course important to know for managing heat in photocathodes. To compute lattice thermal conductivity, we used the anharmonic third-order IFCs. Utilizing the same $1 \times 3 \times 1$ supercell and $2 \times 1 \times 2$ Monkhorst–Pack k-mesh as in Section IV, we got these anharmonic third-order IFCs, considering interactions up to fourth nearest neighbors. Additionally, we obtained the dielectric tensor and Born effective charges based on DFPT to account for long-range electrostatic interactions. The high-frequency dielectric tensor exhibits slight anisotropy with $\epsilon_{xx} = 4.09$, $\epsilon_{yy} = 4.06$, and $\epsilon_{zz} = 4.13$. The computed diagonal Born effective charges are (1.21, 1.30, 1.15) for Cs_I, (1.04, 0.96, 1.12) for Cs_{II}, and (-2.26, -2.25, -2.28) for Te in units of electron charge. The off-diagonal components are lower than 0.1 and not reported here. The positive Born effective charge for Cs atoms and the negative Born effective charge clearly indicate the ionic nature of the bonds in Cs₂Te. The intrinsic lattice thermal conductivity can be calculated by solving the phonon BTE as implemented in ShengBTE code[25] that considers the phonon-phonon scattering processes.

The calculated lattice thermal conductivity of Cs₂Te is shown in [Figure 3\(a\)](#), revealing slight anisotropy along different directions. As temperature increases, phonon scattering intensifies, leading to a decrease in lattice thermal conductivity. At 300 K, the average thermal conductivity of Cs₂Te is predicted to be ~ 0.2 W/(m*K), calculated as the average of thermal conductivities along the three crystallographic axes. This low lattice conductivity places Cs₂Te among the materials with ultralow lattice thermal conductivity.[26] In comparison, Cu photocathodes have a thermal conductivity of ~ 401 W/(m*K) at room temperature.[27] The low thermal conductivity of Cs₂Te photocathodes implies that heat generated in photocathodes by either

illuminating lasers or joule heating, cannot be efficiently dissipated. This deficiency can lead to localized heating and vibrations that may affect quality of generated electron beams. Thus, active cooling methods may be required when operating Cs_2Te photocathodes under high gradients.

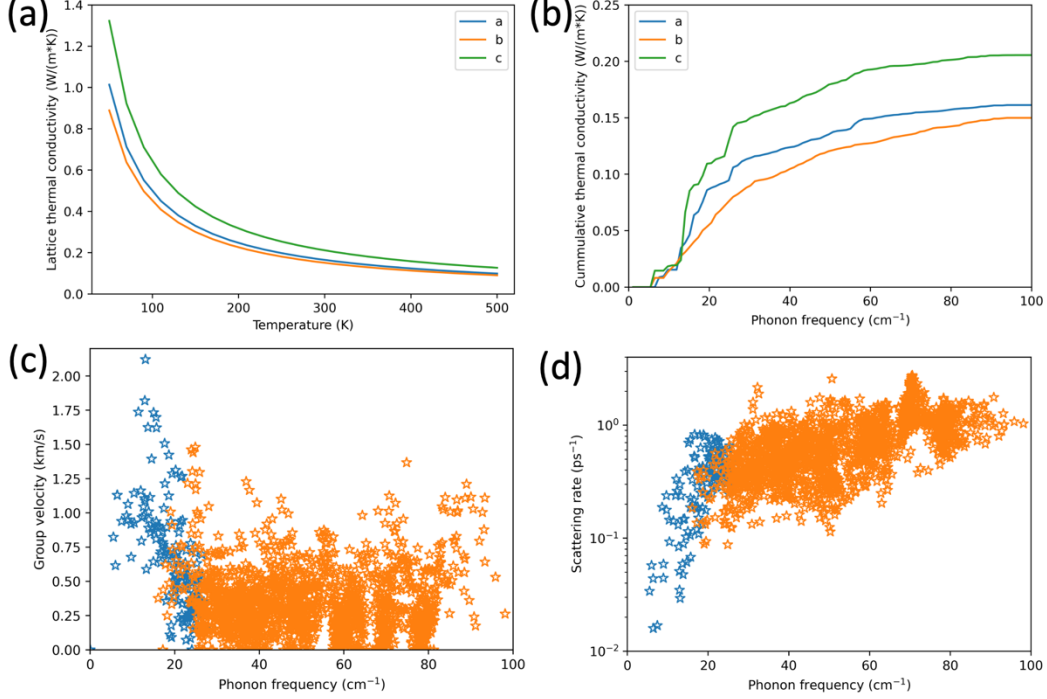


Figure 3. (a) Lattice thermal conductivity, (b) cumulative lattice thermal conductivity, (c) group velocity, and (d) phonon scattering rate of Cs_2Te at 300 K. The acoustic and optical modes are illustrated with blue and orange stars, respectively.

The cumulative thermal conductivity as a function of phonon vibrational frequency of Cs_2Te at 300 K is shown in [Figure 3\(b\)](#). It is seen that phonons with frequencies below 20 cm^{-1} , namely the acoustic phonons, contribute to nearly 50% of the lattice thermal conductivity. In the frequency range of 20-40 cm^{-1} , where acoustic and optical phonons interact, more than 20% of thermal conductivity is contributed. Therefore, the thermal conductivity of Cs_2Te is mainly determined by acoustic phonons and low frequency optical phonons. The maximum mean free path (MFP) of phonons is close to 100 nm and phonons with MFP less than 30 nm contribute 70% to the thermal conductivity. To further clarify the microscopic mechanism behind the ultralow lattice thermal conductivity for Cs_2Te , we plotted the group velocity and phonon-phonon scattering rates ([Figures 3\(c, d\)](#)). The plots show that low-frequency acoustic phonons exhibit higher group velocity and lower scattering rates, while optical phonons have high scattering rates and low group velocities, thus contributing less to thermal conductivity. The overall low lattice thermal conductivity results from the heavy atomic mass of Cs, and the relatively weak chemical bonds between Cs and Te as seen from the small bulk and shear moduli of Cs_2Te in [Section III](#).

VI. Electronic structure of Cs₂Te

The calculated band structure of Cs₂Te with GGA-PBE functional is shown in Figure 4(a). The calculated band gap is ~ 1.7 eV, notably lower than the experimental value of ~ 3.3 eV.[28] Our results align with previous DFT calculations.[29] It is acknowledged that the GGA-PBE functional tends to underestimate band gaps of semiconducting materials.[30] However, despite this limitation, the band dispersion obtained with GGA-PBE functional is similar to that calculated from more advanced functionals, such the HSE06 hybrid functional.[29] Therefore, we anticipate that GGA-PBE functional accurately captures the effective masses and group velocities of electrons and holes, which determine their transport properties. From the band dispersion, the calculated effective masses for electrons are $0.267m_0$, $0.270m_0$, and $0.267m_0$ along the Γ -X, Γ -Y, and Γ -Z directions, respectively, where m_0 is the rest mass of an electron. Much larger effective masses are observed for holes, which are $-2.524m_0$, $-0.732m_0$, $-1.900m_0$, along the Γ -X, Γ -Y, and Γ -Z directions, respectively.

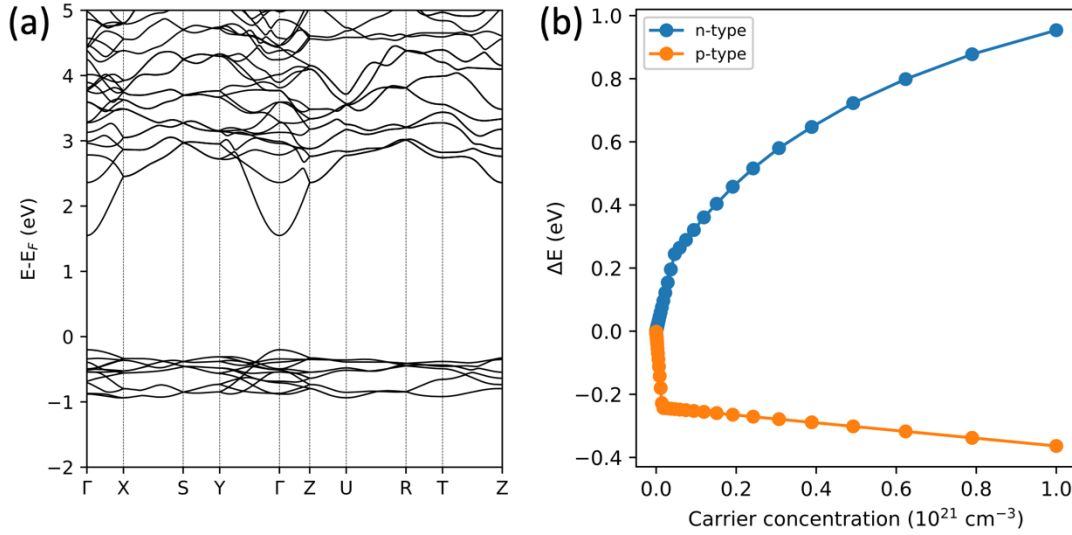


Figure 4. (a) Electronic band structure, and (b) Burstein-Moss energy shift as a function of carrier concentration of Cs₂Te. Positive shifts for electrons, and negative shifts for holes.

The change of the Fermi level as a function of carrier concentration due to Burstein-Moss effect can be calculated using[31, 32]

$$\Delta E = \frac{h^2}{8\pi^2 m^*} (3\pi^2 n)^{2/3}, \quad (1)$$

where h is Planck's constant, and n is the concentration of charge carriers (electrons or holes) associated with the doping level of semiconductors. The energy shifts caused by excess electrons are calculated relative to the conduction band minimum (CBM), and those induced by excess holes are referenced to the valance band maximum (VBM). Figure 4(b) depicts the shifts of the Fermi level as a function of carrier concentration of electrons (n-type) and holes (p-type) in Cs₂Te. With an electron concentration of 10^{21} cm⁻³, the Fermi level is observed to shift 0.8 eV above CBM, whereas with a same hole concentration, it shifts only 0.4 eV below VBM. This difference arises from the narrower dispersion of the valance bands compared to

the conduction bands, as evidenced by the band structure. The transport properties of electrons and holes are evaluated within the carrier concentration range of 10^{18} cm^{-3} (slightly doped Cs_2Te) to 10^{21} cm^{-3} (heavily doped Cs_2Te).

VII. Electron-phonon scattering and carrier mobility in Cs_2Te

In order to gain fundamental understanding of the electron transport properties in Cs_2Te at high electromagnetic fields, we investigated the electron-phonon scattering. We calculated the electron transport properties with the ab-initio scattering and the transport method implemented in the AMSET code.[33, 34] The package solves the electronic BTE in the momentum relaxation-time approximation (MRTA) to calculate scattering rates and mobilities within the Born approximation. In AMSET code, the relaxation time is estimated by the number of different band and k -point dependent scattering rates instead of the constant relaxation-time approach. In this work, we calculated scattering rates by considering the following scattering processes: (a) acoustic deformation potential (ADP), which is responsible for the phonon-electron interactions; (b) ionized impurity (IMP) scattering, which represents scattering of charge carriers by ionization of the lattice; and (c) polar optical phonon (POP) scattering, which considers the interaction between polar optical phonons and electrons. The resulting carrier relaxation time, namely the inverse of the scattering rate τ , was calculated by Matthiessen's rule[33]

$$\frac{1}{\tau} = \frac{1}{\tau^{ADP}} + \frac{1}{\tau^{IMP}} + \frac{1}{\tau^{POP}}, \quad (2)$$

where τ^{ADP} , τ^{IMP} , and τ^{POP} are the relaxation times from the ADP, IMP, and POP scattering, respectively. In ADP and IMP scatterings, electrons do not acquire or lose energy while undergoing elastic scattering, whereas POP scatterings exhibit inelastic scattering that occurs due to phonon emission or absorption. The Fermi's golden rule is used to calculate the scattering rates for elastic and inelastic scattering from an initial $|nk\rangle$ state to the final $|mk+q\rangle$ state. The scattering rate can be written as

$$\tau_{nk \rightarrow mk+q}^{-1} = \frac{2\pi}{\hbar} |g_{nm}|^2 \delta(\epsilon_{nk} - \epsilon_{mk+q}), \quad (3)$$

where ϵ_{nk} and ϵ_{mk+q} are the energy of the initial state and the final state after scattering, g_{nm} is the electron-phonon coupling matrix element that is defined as

$$g_{nm}(\mathbf{k}, \mathbf{q}) = \langle m\mathbf{k} + \mathbf{q} | \Delta_q V | n\mathbf{k} \rangle, \quad (4)$$

where $\Delta_q V$ is the electronic perturbation from different scattering mechanisms. The required parameters to obtain the scattering rates, such as dense and uniform band structures, elastic coefficients, wave-function coefficients, deformation potentials, static and high-frequency dielectric constants, and polar-phonon frequency, were calculated from DFT and DFPT.

The calculated electron and hole scattering rates at 300 K are shown in [Figures 5\(a, b\)](#). The figures show that the POP scattering clearly dominates due to the pronounced polarity of the chemical bonds in Cs_2Te . The ADP scattering and IMP scattering rates have much smaller contributions to the total scattering rates. The electron scattering rate is around 450 ps^{-1} near

the CBM (Figure 5(b)). The hole scattering rate at VBM is around 850 ps^{-1} . These calculated scattering rates were used to calculate the carrier transport and to predict the breakdown field of Cs_2Te .

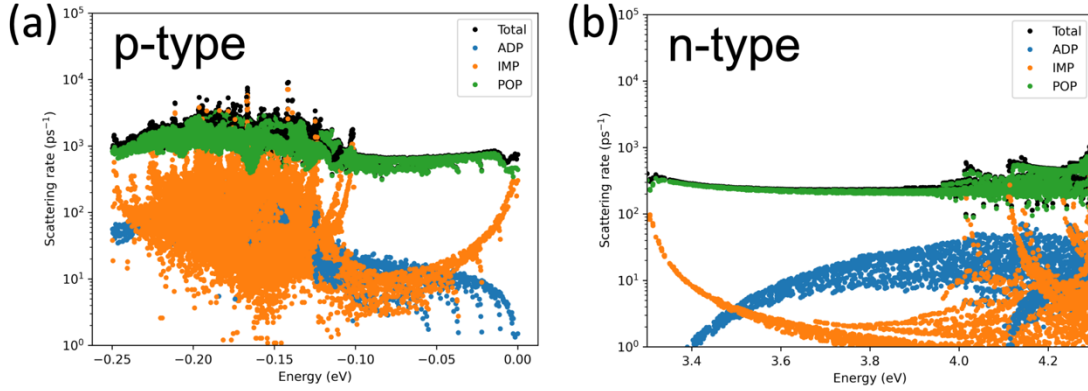


Figure 5. Electron-phonon scattering rates for (a) p-type carrier (holes), and (b) n-type carrier (electrons) of Cs_2Te at 300 K. The carrier concentration is 10^{18} cm^{-3} . Black dots are the total scattering rates. Green, orange, and blue dots represent the contribution from POP, ADP, and IMP scattering, respectively. The Fermi level is set to 0 eV. Negative energy in (a) is related to holes, and positive energy in (b) is related to electrons. A scissor correction is added to shift the CBM to experimental value of 3.3 eV.

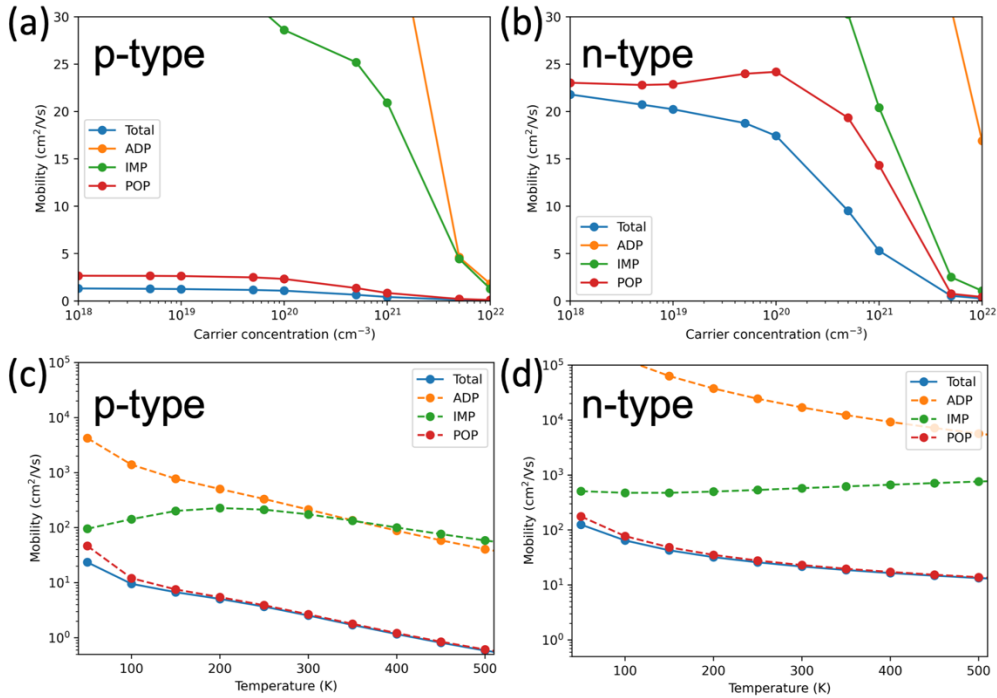


Figure 6. (a, b) Carrier mobility as a function of carrier concentration for p-type (holes) and n-type (electrons) carriers in Cs_2Te at 300 K. (c, d) Carrier mobility as a function of temperature with a carrier concentration of 10^{18} cm^{-3} .

The calculated hole and electron mobilities as functions of temperature and carrier concentrations are shown in Figure 6. In the slightly doped Cs_2Te with an electron concentration

of 10^{18} cm^{-3} , the hole mobility is $\sim 2.0 \text{ cm}^2/(\text{V}\cdot\text{s})$ at 300 K (Figure 6(a)), and the electron mobility is around $20 \text{ cm}^2/(\text{V}\cdot\text{s})$ (Figure 6(b)). Both electron and hole mobilities slightly decrease with carrier concentrations up to 10^{20} cm^{-3} , and rapidly decrease when the carrier concentration is larger than 10^{20} cm^{-3} . Hole and electron mobilities also decrease with temperature as seen from Figures 6(c, d), due to the increased scattering rates at higher temperatures. The much lower mobility of holes than that of electrons is related to the larger scattering rates and the large effective masses of holes.

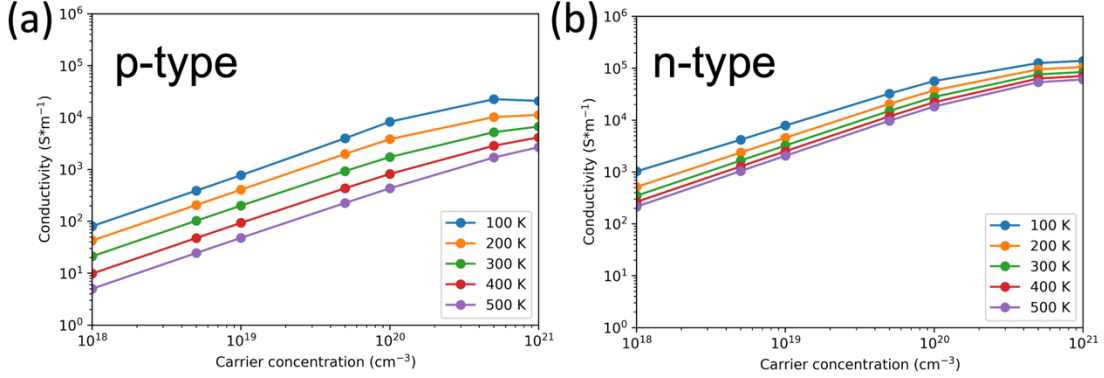


Figure 7. Electrical conductivity of (a) p-type and (b) n-type Cs_2Te as a function of carrier concentrations at different temperatures.

Figures 7(a, b) show calculated electrical conductivities of p-type and n-type doped Cs_2Te . Both p-type and n-type conductivities increase monotonously with carrier concentration from 10^{18} cm^{-3} to 10^{21} cm^{-3} . The increase of conductivities with carrier concentrations is due to the increase in the number of carriers participating in the conduction process. The electrical conductivities decrease with temperature, which can be attributed to the increased electron-phonon scattering rates at higher temperatures. Moreover, it is seen that the n-type conductivity is around one order of magnitude larger than the p-type conductivity at the same carrier concentration and temperature.

VIII. Dielectric breakdown in Cs_2Te

The dielectric breakdown field of Cs_2Te is estimated via a fully first-principles approach based on the Frohlich-von Hippel criterion.[10, 35, 36] This method contemplates that an electron avalanche occurs when the electron energy reaches the threshold to excite a valence electron across the electronic energy gap, causing electron multiplication and leading to impact ionization. The dielectric breakdown occurs when the rate of energy gain $A(E, \epsilon, T)$ of an electron with energy ϵ due to the external field E at temperature T is larger than the energy-loss rate $B(\epsilon, T)$ due to electron-phonon scattering

$$A(E, \epsilon, T) > B(\epsilon, T), \quad (5)$$

for energies ϵ ranging from CBM to the impact ionization threshold of $\text{CBM} + E_g$, where E_g is the band gap of the material.[10, 36-38] The energy-gain rate of the electron can be evaluated as

$$A(E, \epsilon, T) = \frac{1}{3} \frac{e^2 \tau(\epsilon, T)}{m^*} E^2, \quad (6)$$

where e and m^* are the electronic charge and effective mass, respectively. $\tau(\epsilon, T)$ is the energy- and temperature-dependent electron-phonon scattering rate, as shown in Figure 5(b). The field-independent rate of energy loss $B(\epsilon, T)$ to the lattice is obtained by subtracting the rate of phonon absorption from phonon emission[36]

$$B(\epsilon, T) = \frac{2\pi}{\hbar D(\epsilon)} \sum_{\pm} \sum_{nk} \sum_{mk+q} \left\{ \begin{array}{l} \pm \hbar \omega_q |g_{nm}(\mathbf{k}, \mathbf{q})|^2 \left(n_q + \frac{1}{2} \mp \frac{1}{2} \right) \\ \times \delta(\epsilon_{nk} - \epsilon_{mk+q} \pm \hbar \omega_q) \delta(\epsilon_{nk} - \epsilon) \end{array} \right\}, \quad (7)$$

where n_q is the phonon occupation number that is given by Bose-Einstein distribution, \pm sign represents the adsorption and emission of phonon, respectively, and ω_q is the phonon frequency. We used an effective phonon frequency that is defined as the weighted sum over all phonon modes at Γ -point.[33] In Figure 8(a) we present the energy loss rate as a function of energy (black line) and energy gain rate under different external fields (blue lines), starting from the CBM. The intrinsic breakdown field is defined as the smallest external electric field such that the energy gain rate is larger than the energy loss rate for all energies between the CBM and the CBM plus the band gap (3.3 eV). We found that that the breakdown field is ~ 60 MV/m at room temperature for Cs_2Te with an electron concentration of 10^{18} cm^{-3} . Using the same approach, we obtained the breakdown fields for different carrier concentrations and temperatures as shown in Figure 8(b). The breakdown field clearly increases with temperature and higher carrier concentrations due to the increased energy loss rate at higher temperatures and higher carrier concentrations. The dielectric breakdown field of Cs_2Te at 300 K is predicted to vary from 60 MV/m to 132 MV/m depending on the doping level of samples. It is to be noted that the von Hippel low-energy criterion should be seen as a lower bound for the breakdown field. This is because Cs_2Te is not available in single-crystalline form since it is grown via deposition methods that give rise to polycrystalline samples with varying grain sizes. The scattering introduced by the grain boundaries may further contribute to energy loss rate and increase the breakdown field. Additionally, the method considers the breakdown due to an applied DC field, which may not be suitable in conditions in RF photoinjectors where photocathodes are exposed to RF fields.

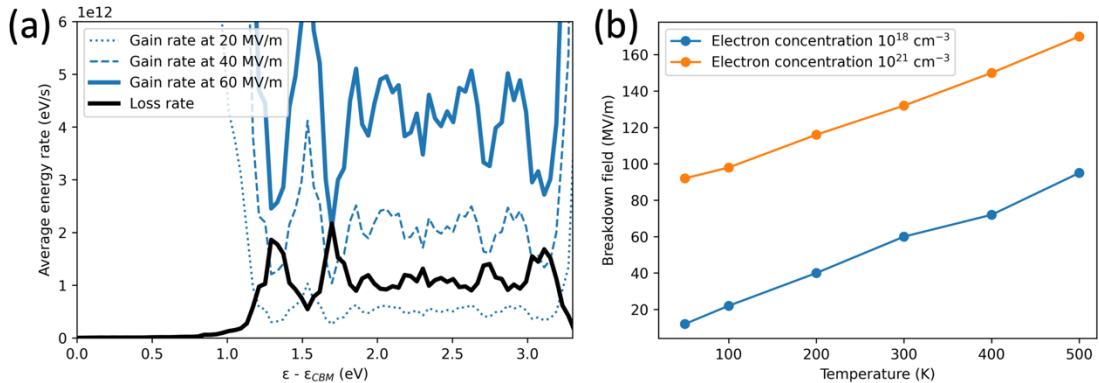


Figure 8. Dielectric breakdown of Cs_2Te . (a) Energy-gain rate $A(E, \epsilon, T)$ from an applied external field and energy loss rate $B(\epsilon, T)$ due to electron-phonon scattering. Both quantities are calculated at 300 K for an electron concentration of 10^{18} cm^{-3} . The intrinsic breakdown occurs when the applied electric field is such that the energy gain rate is larger than the loss rate for all energies between the conduction-band minimum (CBM) and the CBM plus the

energy of the band gap (3.3 eV). (b) The dielectric breakdown field of Cs₂Te as a function of temperature for slightly (10¹⁸ cm⁻³) and heavily (10²¹ cm⁻³) doped Cs₂Te.

IX. Conclusion

This paper reports results of our investigation of the structural, elastic, electronic, vibrational, and transport properties of Cs₂Te using first-principles calculations. We computed the electron-phonon and phonon-phonon scattering rates of Cs₂Te using first-principles approach for the first time, enabling calculations of electron and phonon transport via the Boltzmann transport equation (BTE). We computed material properties of Cs₂Te, such as lattice thermal conductivity, carrier mobilities and conductivities, based on the electron-phonon and phonon-phonon scattering. We predicted the intrinsic electron and hole mobility of Cs₂Te to be 20 and 1.2 cm²/Vs, respectively, at room temperature. The low mobility is explained by the strong polar optical phonon scattering. We predicted that Cs₂Te has ultralow lattice thermal conductivity of 0.2 W/(m*K) at room temperature due to low group velocities and relatively weak bonds in Cs₂Te. Based on the electron-phonon scattering rates and the von Hippel low-energy criterion, the dielectric breakdown field of Cs₂Te is predicted to vary between 60 MV/m 132 MV/m at room temperature, depending on the doping of the material. Our studies serve as a basis for understanding the high-gradient performance of Cs₂Te photocathodes.

Acknowledgements

The authors gratefully acknowledge the funding for this project from the Laboratory Directed Research and Development program of Los Alamos National Laboratory (LANL) under projects 20230011DR and 20230808ER. LANL is operated by Triad National Security, LLC, for the National Nuclear Security Administration of U.S. Department of Energy (Contract No. 89233218CNA000001). This research used resources provided by the Los Alamos National Laboratory Institutional Computing Program.

References

1. Wang, E., et al., *Long lifetime of bialkali photocathodes operating in high gradient superconducting radio frequency gun*. Scientific Reports, 2021. **11**(1): p. 4477.
2. Filippetto, D., et al., *Electron sources for accelerators*. arXiv preprint arXiv:2207.08875, 2022.
3. Baliga, B.J., *Semiconductors for high-voltage, vertical channel field-effect transistors*. Journal of applied Physics, 1982. **53**(3): p. 1759-1764.
4. Hudgins, J.L., et al., *An assessment of wide bandgap semiconductors for power devices*. IEEE Transactions on power electronics, 2003. **18**(3): p. 907-914.
5. Filippetto, D., H. Qian, and F. Sannibale, *Cesium telluride cathodes for the next generation of high-average current high-brightness photoinjectors*. Applied Physics Letters, 2015. **107**(4).
6. Di Bona, A., et al., *Auger and x-ray photoemission spectroscopy study on Cs₂Te photocathodes*. Journal of applied physics, 1996. **80**(5): p. 3024-3030.
7. Monaco, L. and D. Sertore, *REVIEW OF RECENT PHOTOCATHODE ADVANCEMENTS*. 40th International Conference on Free Electron Lasers.
8. Simakov, E., et al. *Update on the status of the C-band high gradient program at LANL*. in *Proceedings of the 14th International Particle Accelerator Conference (IPAC'23), Venice, Italy*. 2023.
9. Schaber, J., R. Xiang, and N. Gaponik, *Review of photocathodes for electron beam sources in particle accelerators*. Journal of Materials Chemistry C, 2023. **11**(9): p. 3162-3179.
10. Von Hippel, A., *Electric breakdown of solid and liquid insulators*. Journal of Applied Physics, 1937. **8**(12): p. 815-832.
11. Gupta, P., L. Cultrera, and I. Bazarov, *Monte Carlo simulations of electron photoemission from cesium antimonide*. Journal of Applied Physics, 2017. **121**(21): p. 215702.
12. Jensen, K.L., *A tutorial on electron sources*. IEEE Transactions on Plasma Science, 2018. **46**(6): p. 1881-1899.
13. Banfi, F., et al., *Monte Carlo Transverse Emittance Study on Cs₂Te*. 27th International Conference on Free Electron Lasers. 2005, p. 572.
14. Perdew, J.P., K. Burke, and M. Ernzerhof, *Generalized gradient approximation made simple*. Physical review letters, 1996. **77**(18): p. 3865.
15. Blöchl, P.E., *Projector augmented-wave method*. Physical review B, 1994. **50**(24): p. 17953.
16. Terdik, J.Z., et al., *Anomalous work function anisotropy in ternary acetylides*. Physical Review B, 2012. **86**(3): p. 035142.
17. Gonschorek, W., *Golden Book of Phase Transitions*. 2002, Wroclaw.
18. Momma, K. and F. Izumi, *VESTA: a three-dimensional visualization system for electronic and structural analysis*. Journal of Applied crystallography, 2008. **41**(3): p. 653-658.

19. Gaillac, R., P. Pullumbi, and F.-X. Coudert, *ELATE: an open-source online application for analysis and visualization of elastic tensors*. Journal of Physics: Condensed Matter, 2016. **28**(27): p. 275201.
20. Mouhat, F. and F.-X. Coudert, *Necessary and sufficient elastic stability conditions in various crystal systems*. Physical review B, 2014. **90**(22): p. 224104.
21. Hill, R., *The elastic behaviour of a crystalline aggregate*. Proceedings of the Physical Society. Section A, 1952. **65**(5): p. 349.
22. Voigt, W., *Lehrbuch der kristallphysik: (mit ausschluss der kristalloptik)*. Vol. 34. 1910: BG Teubner.
23. Reuß, A., *Berechnung der fließgrenze von mischkristallen auf grund der plastizitätsbedingung für einkristalle*. ZAMM-Journal of Applied Mathematics and Mechanics/Zeitschrift für Angewandte Mathematik und Mechanik, 1929. **9**(1): p. 49-58.
24. Togo, A., *First-principles phonon calculations with phonopy and phono3py*. Journal of the Physical Society of Japan, 2023. **92**(1): p. 012001.
25. Li, W., et al., *ShengBTE: A solver of the Boltzmann transport equation for phonons*. Computer Physics Communications, 2014. **185**(6): p. 1747-1758.
26. Lindsay, L., et al., *Survey of ab initio phonon thermal transport*. Materials Today Physics, 2018. **7**: p. 106-120.
27. Yunus, A.C., *Heat transfer: a practical approach*. MacGraw Hill, New York, 2003. **210**.
28. Powell, R., et al., *Photoemission studies of cesium telluride*. Physical review B, 1973. **8**(8): p. 3987.
29. Saßnick, H.-D. and C. Cocchi, *Electronic structure of cesium-based photocathode materials from density functional theory: Performance of PBE, SCAN, and HSE06 functionals*. Electronic Structure, 2021. **3**(2): p. 027001.
30. Chan, M.K. and G. Ceder, *Efficient band gap prediction for solids*. Physical review letters, 2010. **105**(19): p. 196403.
31. Hamberg, I., et al., *Band-gap widening in heavily Sn-doped In₂O₃*. Physical Review B, 1984. **30**(6): p. 3240.
32. Jain, S., J. McGregor, and D. Roulston, *Band-gap narrowing in novel III-V semiconductors*. Journal of applied physics, 1990. **68**(7): p. 3747-3749.
33. Ganose, A.M., et al., *Efficient calculation of carrier scattering rates from first principles*. Nature communications, 2021. **12**(1): p. 2222.
34. Lee, H., et al., *Electron-phonon physics from first principles using the EPW code*. arXiv preprint arXiv:2302.08085, 2023.
35. Fröhlich, H., *Theory of electrical breakdown in ionic crystals*. Proceedings of the Royal Society of London. Series A-Mathematical and Physical Sciences, 1937. **160**(901): p. 230-241.
36. Sun, Y., S. Boggs, and R. Ramprasad, *The intrinsic electrical breakdown strength of insulators from first principles*. Applied Physics Letters, 2012. **101**(13): p. 132906.

37. Sparks, M., et al., *Theory of electron-avalanche breakdown in solids*. Physical Review B, 1981. **24**(6): p. 3519.
38. Sun, Y., et al., *50+ years of intrinsic breakdown*. IEEE Electrical Insulation Magazine, 2013. **29**(2): p. 8-15.